Considerations for the temperature stratification in a pre-burn constant-volume combustion chamber

Experimental Thermal and Fluid Science 144 (2023) 110866

Contents lists available at ScienceDirect

Experimental Thermal and Fluid Science

journal homepage: www.elsevier.com/locate/etfs

Considerations for the temperature stratification in a pre-burn constant-volume combustion chamber

Noud Maes [a,b,*], Fabien Tagliante [a], Hyung Sub Sim [c], Maarten Meijer [b], Julien Manin [a], Lyle M. Pickett [a]

[a] Combustion Research Facility, Sandia National Laboratories, P.O. Box 969, MS 9053, Livermore, CA 94551, USA
[b] Department of Mechanical Engineering, Eindhoven University of Technology, P.O. Box 513, 5600 MB Eindhoven, The Netherlands
[c] Department of Aerospace Engineering, Sejong University, Seoul, Republic of Korea

ARTICLE INFO

Keywords:
Engine Combustion Network (ECN)
Spray A
Temperature measurements
Temperature stratification
Computational Fluid Dynamics

ABSTRACT

In recent years, the Engine Combustion Network (ECN) has developed as a worldwide reference for understanding and describing engine combustion processes, successfully bringing together experimental and numerical efforts. Since experiments and numerical simulations both target the same boundary conditions, an accurate characterization of the stratified environment that is inevitably present in experimental facilities is required. The difference between the core-, and pressure-derived bulk-temperature of pre-burn combustion vessels has been addressed in various previous publications. Additionally, thermocouple measurements have provided initial data on the boundary layer close to the injector nozzle, showing a transition to reduced ambient temperatures. The conditions at the start of fuel injection influence physicochemical properties of a fuel spray, including near nozzle mixing, heat release computations, and combustion parameters. To address the temperature stratification in more detail, thermocouple measurements at larger distances from the spray axis have been conducted. Both the temperature field prior to the pre-combustion event that preconditions the high-temperature, high-pressure ambient, as well as the stratification at the moment of fuel injection were studied. To reveal the cold boundary layer near the injector with a better spatial resolution, Rayleigh scattering experiments and thermocouple measurements at various distances close to the nozzle have been carried out. The impact of the boundary layers and temperature stratification are illustrated and quantified using numerical simulations at Spray A conditions. Next to a reference simulation with a uniform temperature field, six different stratified temperature distributions have been generated. These distributions were based on the mean experimental temperature superimposed by a randomized variance, again derived from the experiments. The results showed that an asymmetric flame structure arises in the computed results when the temperature stratification input is used. In these predictions, first-stage ignition is advanced by 24 μs, while second-stage ignition is delayed by 11 μs. At the same time a lift-off length difference between the top and the bottom of up to 1.1 mm is observed. Furthermore, the lift-off length is less stable over time. Given the shown dependency, the temperature data is made available along with the vessel geometry data as a recommended basis for future numerical simulations.

1. Introduction

Experimental setups that simulate a wide variety of high-pressure and high-temperature ambient environments are widely used to aid in understanding fuel spray mixing, combustion, and emission characteristics of internal combustion engines [1–4]. Such dedicated test rigs typically provide superior optical access in a quiescent environment with a more homogeneous temperature stratification when compared to an internal combustion engine. In many cases they are favored by numerical efforts as a reference due to these simplifications, and the associated well-defined boundary conditions.

Several types of experimental setups are capable of reaching ambient conditions representative of those found in an internal combustion engine [1]. The most common facilities that can cover a large range of operating conditions, however, are the constant-volume pre-burn chamber and the constant-pressure constant-flow designs [3,4]. In a constant-flow design, ambient gases are continuously compressed, heated, and fed through a test section. In a constant-volume pre-burn

* Corresponding author at: Department of Mechanical Engineering, Eindhoven University of Technology, P.O. Box 513, 5600 MB Eindhoven, The Netherlands.
E-mail address: n.c.j.maes@tue.nl (N. Maes).

https://doi.org/10.1016/j.expthermflusci.2023.110866
Received 15 November 2022; Received in revised form 22 January 2023; Accepted 26 January 2023
Available online 6 February 2023

combustion vessel, a pre-mixed charge is ignited to produce high-temperature and high-pressure gases. Pressure and temperature rise during the premixed combustion, and then gradually decrease due to heat losses to the walls. Eventually, the pre-defined target conditions are reached in the core of the chamber and fuel is injected.

Combustion and emission formation characteristics in internal combustion engines are particularly dependent on ambient temperature, which has led researchers to measure the gas temperature at the location where the flame will ignite and stabilize [2,3,5–7]. As chambers are designed such that the fuel spray mixes with gases towards the chamber center, the ambient gases that mix with the spray have become known as the "core" gases. For a constant-volume pre-burn combustion chamber, such as the one discussed in this work, a relationship between the measured core temperature and the pressure-derived bulk temperature can be determined. Typically, the relationship is determined without fuel injection, and the pressure-derived bulk temperature can subsequently be used in experiments with spray flames to predict the corresponding core temperature for every single repetition. The difference between the core and bulk temperature arises from crevices and boundary layers near the walls, as well as a buoyancy driven temperature stratification. Additionally, flow driven structures caused by an internal mixing fan may exist. Although a mixing fan is typically operated to reduce the buoyancy and boundary layer effects, it may still introduce other perturbations of temperature (or density).

The combustion vessel discussed in this work has been operational since 1997, providing fundamental spray analyses that are often used for numerical simulations (e.g [8–13]). In 2009, the combustion vessel became one of the reference setups for the Engine Combustion Network (ECN) [14,15]. Along with other combustion vessels within the ECN, the ambient environment in the center of the chamber was characterized in detail to achieve consistent results among different setups [3]. However, not much attention was given to the boundary layers that inherently develop close to the vessel walls, and their effect on fuel sprays. With increasing computational performance, accuracy, and capabilities, inclusion of any non-uniformities in initial conditions, including thermal boundary layers should be considered as one of the next steps forward. The air entrained by a fuel spray is drawn in from surrounding regions, including those perpendicular to the spray axis or even upstream of the nozzle tip [16–20]. In the near-nozzle region, this means that the entrained gases originate from the cooler boundary layers, directly influencing mixing processes. Although this work specifically targets a pre-burn combustion chamber, boundary layers will exist in all combustion systems relevant to internal combustion engines. More importantly, the combustion vessel and injector mounting in this work were developed and are operated in such a way that these boundary layers and buoyancy effects are minimized. Therefore, non-uniform temperature effects are expected to be exacerbated when different combustion systems are considered.

The application of accurate gas temperature measurements in a combustion environment limits the available techniques to thermocouples, or non-intrusive light-based diagnostics [21]. Thermocouples have traditionally been used to characterize the core temperatures of pre-burn vessels [2,3,5–7], while Rayleigh scattering was used to measure vapor-phase fuel concentration and temperature in a high-temperature ambient using the assumption of adiabatic mixing [22–24]. Thermocouple measurements are relatively easy to implement and allow high-speed acquisition provided that the wires are sufficiently thin. However, they are limited to at most several individual measurement points and might disturb the internal gas flow and cool-down behavior of the combustion vessel through differences in heat losses and vessel volume. With a known gas composition, the corrected Rayleigh signal is inversely proportional to temperature [22], providing a 2D temperature distribution via the number density of the ambient gas. It does, however, require a reference temperature or number density which necessitates additional measurements with thermocouples after all.

In this work, thermocouple- and Rayleigh scattering measurements are used to characterize the temperature history and stratification found in a pre-burn combustion vessel. Particular focus is given to the stratification at the moment that fuel would be injected, and to the boundary layer in the near nozzle region. The direct effect of the boundary layer on reacting fuel jets cannot be determined experimentally since they are inevitable in a high-temperature ambient combustion environment. Therefore, complimentary Computational Fluid Dynamics (CFD) simulations performed in the CONVERGE framework are used in this work to illustrate the importance of these boundary layers on characteristic combustion parameters such as ignition delay and lift-off length. To promote the usage of actual temperature stratification effects in future CFD simulations, 3D temperature maps of the combustion vessel are made available on the ECN website [15].

2. Experimental methods

2.1. Constant-volume combustion vessel

The optically accessible combustion vessel used in this work has a cubical shaped combustion chamber with 108-mm edges. The vessel walls are electrically heated to 461 K. A fuel injector is located in a metal port in one of the faces of the combustion chamber, while another face hosts two custom spark plugs that initiate the pre-burn. In addition to the face ports, 19-mm diameter corner ports are used for an internal mixing fan (spinning at 1000 rpm), inlet and outlet valves, and pressure- and temperature sensors. Surface file models with the internal vessel geometry and injector position are available to download at [25] Following the pre-burn of an acetylene, hydrogen, oxygen, and nitrogen mixture, combustion products cool down during a relatively long cool-down period (~3 s). At the pre-computed target conditions, the fuel injector is triggered, and injection, vaporization, and combustion processes ensue. More information on the combustion chamber and its operation can be found in previous publications [2,26,27]. In this work, however, fuel is not injected as the aim of the experiments is to characterize the temperature distribution in the combustion chamber in more detail.

2.2. Type-R thermocouple measurements

The gas temperature inside the combustion chamber was measured during the pre-burn and cool-down period, using two different type-R thermocouple assemblies, see Fig. 1. Note how the axes in the vessel are defined such that y corresponds to the vertical axis, and x is defined along the injector orifice spray axis with z in the same horizontal plane. In previously reported work, an adjustable probe with five fine wire (50-μm diameter) thermocouples suspended between 250-μm support wires (left illustration in Fig. 1) was used to measure the temperature in seven axial locations between 1–67 mm from the injector nozzle [2]. In this work, additional measurements are carried out close to the spray nozzle with the same translatable five-thermocouple probe, now spanning the range between 0.5–8.0 mm from the injector orifice. Away from the spray axis, slightly different axial distances were achieved due to the probe- and conical injector window shape. With the injector tip/port protruding in an 18° half-angle cone, thermocouples may reach negative axial distance values off of the injector axis.

The illustration on the right-hand side of Fig. 1 shows a second assembly with three individual bare wire thermocouple probes. This assembly is used to measure gas temperatures farther away from the spray axis at an axial distance of 45 mm from the injector orifice. The thermocouples enter the vessel such that one is placed at the spray axis (z = 0 mm, y = 0 mm), one is at a radial distance of +25 mm, and a "bent" TC has a shaft position of −42 mm. However, this outer thermocouple is subsequently bent by an additional distance of approximately 7.4 mm, outward towards the vessel boundary layer (to an optically confirmed y or z = +/−50.4 mm). In this work, the

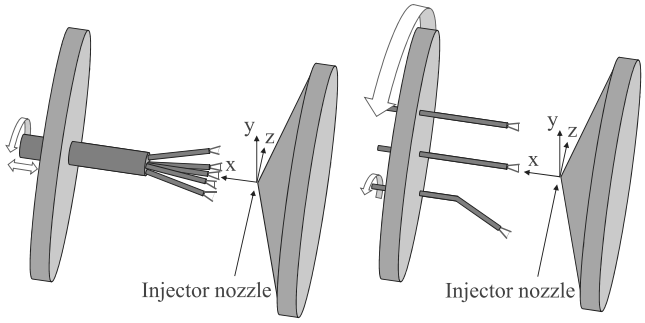

Fig. 1. Left: adjustable probe with five 50-μm diameter type-R thermocouples. Right: three individual single bare-wire type-R thermocouple probes.

port containing the three probes is rotated in 90° steps, while at each of those position the bent thermocouple is rotated in 180° steps (essentially moving the thermocouple inward towards the spray axis to achieve an optically confirmed radial distance of 35.5 mm). This way, eight unique measurement configurations are obtained. In the horizontal (x-z) plane, a laser sheet entrance window, with dimensions of 63 mm in the x direction and 17 mm in the y direction, locally protrudes in the z direction about 3 mm away from the wall of the vessel to z = +51 mm. Therefore, the outermost thermocouple recorded boundary layer temperatures at a distance of 0.6 mm from the window at that location, while at other rotations the distance from the window ports is about 3.6 mm. The 5-kHz type-R thermocouple signals were conditioned, amplified, low-pass filtered with a cut-off of 100 Hz, and averaged to characterize the flame temperatures, and gas temperatures during the entire pre-burn and cool-down process. Corrections were made for the radiation and convection of the thermocouple beads, see [2] for more details.

Having temperature history available at multiple locations, initial vessel conditions (prior to the spark-initiated pre-burn), compression heating, flame arrival, maximum flame temperature, and cool down behavior are studied. The main aim, however, is to know the temperature stratification at the moment of fuel injection.

2.3. Rayleigh scattering

The 2D temperature stratification of the constant-volume combustion vessel at a targeted 900-K ambient temperature is studied in the horizontal (x-z) plane at the height of the injector nozzle (y = 0 mm) using Rayleigh scattering, similar to previous work [22,24]. A 2D optical measurement of temperature provides additional information on mean and variance, rather than the limited measurement by thermocouples in only a few positions. The second harmonic of a Nd:YAG laser at 532 nm with a pulse energy of 150 mJ and a pulse duration of seven nanoseconds was used to create a 30-mm wide laser sheet with a thickness of about 300 μm. The laser sheet was translated over the horizontal plane towards the injector orifice, up to a distance of about 0.4 mm from the nozzle. Rayleigh scattered light was collected from the bottom window of the combustion vessel with a back-illuminated CCD camera (PIXIS 1024B) through a 532-nm narrow-band-pass filter (10-nm FWHM). Three laser sheet locations were used to cover a region of about 70 × 80 mm.

Flare images were captured with the laser sheet polarization rotated and at low vessel pressure, preventing collection of Rayleigh scattered light from gas molecules, but allowing scatter from surfaces within the chamber to be collected. Additional flare was measured just outside of the laser sheet (from background surfaces) for conditions at pressure when there are more molecular scattering events or instances, and the two were combined to create a background flare image. Subtracting these images from the Rayleigh scattering images successfully removed the flare such that the Rayleigh signal depends on the signal collection efficiency η, the laser intensity I_l, the total number density N, the mole fraction X_i, and the Rayleigh cross-section σ_i of the species i according to

$$I_R = \eta I_l N \sum_i X_i \sigma_i. \tag{1}$$

Because of the relatively long cool-down time and internal mixing fan, a single gas composition can be assumed at the time of injection. The Rayleigh signal therefore directly relates to local variations of number density and laser sheet intensity. When the laser sheet intensity distribution is known, the Rayleigh signal is inversely proportional to temperature. In previous thermocouple experiments, it was shown how the temperature distribution does not vary significantly in a horizontal plane near the spray axis [2]. Using this information, the laser sheet intensity distribution can be interpolated based on regions inside that vessel that are expected to be invariant in terms of temperature variations. With this calibration for laser sheet intensity, regions of non-uniformity in temperature may be revealed.

3. Numerical methods

To illustrate the importance of characterizing the temperature stratification in a combustion chamber, with implications on CFD methodology, complimentary spray simulations were performed using Reynolds-Averaged Navier–Stokes (RANS) computations. The experimental results presented in this study were used as an input to create a variable temperature grid of the constant-volume vessel which includes boundary layers.

In the numerical study, two types of initial temperature profiles have been used: a conventional uniform temperature profile and a stratified temperature profile based on the experimental measurements as detailed below. The latter takes into account the mean stratified temperature in the chamber as well as the realization-to-realization variance observed in the experiments. A total of six stratified temperature profiles have been modeled by varying the seed number. More details on the modeling of the stratified temperature profile are provided in Section 4.2. The simulations were carried out with the CONVERGE CFD code, version 3.0. Using uniform or stratified temperature profiles, RANS simulations under non-reacting and reacting conditions were performed.

The ECN Spray A conditions are investigated in this numerical study [15]. N-dodecane is injected through the new Spray A-3 injector at 150 MPa [37], in a computational domain representative of the real vessel geometry (illustrations of the geometry can be found in Refs. [25, 38]). The Spray A-3 nozzle is characterized by a slightly larger orifice diameter (94 μm) and greater discharge coefficient (0.937) compared to the original Spray A nozzle. A long injection duration of 3.4 ms (9.9 mg of fuel) is used to capture the spatial flame variation response when changing the initial gas temperature profile. The physical time simulated for all the simulations is five milliseconds.

Both fixed cell embedding, and adaptive mesh refinement (AMR) are used to refine the mesh. The fixed embedding zone is a 7-mm long frustum centered on the spray axis, with an initial radius of 1 mm at the nozzle tip and a maximum radius of 2 mm downstream. For more details on the numerical setup, the reader can refer to Table 1. The improved parallelization of CONVERGE 3.0 compared to version 2.4 allows the user to achieve a maximum grid resolution of 0.125 mm at an affordable CPU cost. Note that this is twice the resolution when compared to the majority of Spray A RANS simulations found in literature [8,39–41]. Another novelty of this study is the use of the corrected distortion spray model [32], which has shown improved prediction of the liquid-phase vaporization. Moreover, OH* reactions (chemically excited OH radicals), extracted from the Aramco 2.0 mechanism [42], are added to the Yao mechanism to accurately compare the methodology for lift-off length and the ignition delay values between experiments

Table 1
Details of the numerical setup used in this work.

Numerical setup	
CFD code	CONVERGE V3.0
Computational domain	Constant-volume vessel
Type grid	AMR and fixed embedding
Base grid [mm]	4
Embedding level for AMR & fixed embedding	5
Maximum grid resolution [mm]	0.125
Models	
Turbulence	RANS k-ϵ STD
Droplet type	Lagrangian parcel
Breakup model	KH-RT [28,29]
Vaporization	Frössling [30,31] + [32]
Droplet collision	No time counter (NTC) [33]
Droplet drag	Dynamic sphere [34] + [32]
Droplet dispersion	O'Rourke [30]
Initial droplet diameter	94 μm
Number of parcels	2,048,000
Cone angle	21° [24]
Combustion model	SAGE [35]
Chemical mechanism	Yao [36] + OH* (Table A.3)
Initial conditions	
Temperature [K]	900 with/without stratified profile
Pressure [bar]	60
Initial turbulent kinetic energy (TKE) [m^2/s^2]	5.02e−4
Initial TKE dissipation rate [m^2/s^3]	1.96e−2
Initial velocity (x, y, z) [m/s]	(0.0287, 0.0078, 0.01825)
Non-reacting mass fractions: Y_{N_2}, Y_{O_2}, Y_{CO_2}, Y_{H_2O} [–]	0.876, 0.000, 0.100, 0.024
Reacting mass fractions: Y_{N_2}, Y_{O_2}, Y_{CO_2}, Y_{H_2O} [–]	0.720, 0.164, 0.094, 0.022

and simulations [36]. A details the reactions and the rate coefficients associated for each new reaction added to the Yao mechanism.

In the numerical simulations, particular attention is given to initial velocity, turbulence, and temperature conditions inside the combustion vessel. Particle image velocimetry measurements, performed in a previous study by Sphicas et al. [19], have determined the average velocity and fluctuation in the horizontal (x) and vertical (y) directions equal to $\overline{U_x} = 0.0287$ m/s, $\overline{U_y} = 0.0078$ m/s, $RMS_x = 0.0168$ m/s, and $RMS_y = 0.0197$ m/s, respectively. Assuming that the average velocity and the fluctuation in the z-direction can be approximated by averaging the values obtained in the x- and y-directions, the turbulent kinetic energy (TKE or k) is estimated as 5.02e−4 m^2/s^2. Table 1 shows the initial velocity, turbulent kinetic energy and TKE dissipation rate imposed in the computational domain based on the experimental observations. The TKE dissipation rate is computed using the following equation:

$$\epsilon = \frac{C_\mu^{3/4} k^{3/2}}{l_t}, \tag{2}$$

where C_μ is the turbulent viscosity coefficient (equal to 0.009) and l_t is the hydraulic diameter of the injector (94 μm).

Despite the use of actual measured boundary conditions for TKE, we note that RANS modeling for Spray A has been shown to have certain weaknesses in mixing and turbulence, particularly when compared to LES. In general, RANS predictions for Spray A show a jet that is more diffuse downstream and with slower penetration compared to the experiment, while LES shows better experimental agreement on jet radial mixture fraction profiles and vapor penetration [32]. In addition, RANS simulations show a high degree of sensitivity to the initial TKE, with some opting to use higher TKE (than measured in the quiescent chamber) as a "necessary" condition for the RANS modeling assumption itself [43]. Despite some limitations, RANS simulations may still provide critical guidance with lower computational expense.

4. Results and discussion

4.1. Experimental results

For both thermocouple- and Rayleigh scattering data, ten experiments were targeted for each measurement point. In some exceptions, however, only three realizations where achieved, which may be reflected by the 95% confidence intervals shown in the following figures. Using the time-resolved thermocouple data, first the initial vessel temperature is discussed. This data is measured after the filling process in which the pre-burn charge is administered to the vessel until the target pressure is reached. After spark ignition of the charge, the evolution of temperature during the pre-burn and cool-down period are evaluated, studying flame arrival, maximum temperatures, and the effects of flame temperature and compression heating. Eventually, the temperature distribution at the time of injection for a 900-K target ambient is studied based on thermocouple- and Rayleigh scattering data.

4.1.1. Initial vessel temperature

After administering the pre-burn charge to the combustion vessel, high-speed pressure and temperature measurements commence and two sparks initiate the pre-combustion. When attempting to simulating this entire pre-burn event with a given oxygen concentration target (see [44]), it is recommended to use the initial conditions provided here. The temperature in the horizontal plane at the time of the spark discharge is represented in Fig. 2. The top panel shows how temperatures fluctuate 5 to 10 K throughout the vessel, with the 95% confidence intervals indicating that these differences are not significant. Green markers represent predicted temperatures, based on the assumption of a symmetric temperature profile around z = 0 mm. However, the laser entrance window on the right visibly protrudes into the combustion chamber. Therefore, predictions of temperature are based on the distance from the vessel windows when measurements are taken within the expected boundary layer thickness. Note that the vessel walls are electrically heated to 461 K, but that the faces and corner ports of the cube are not heated, leading to a lower wall- and gas temperature overall.

The central panel shows a similar temperature stratification in vertical direction. In this case there are, however, slightly lower temperatures in the bottom of the vessel when compared to the top, which is most likely related to buoyancy.

The bottom panel of Fig. 2 shows how a temperature drop of about 5 K is present on the spray axis in the near nozzle region. In this case,

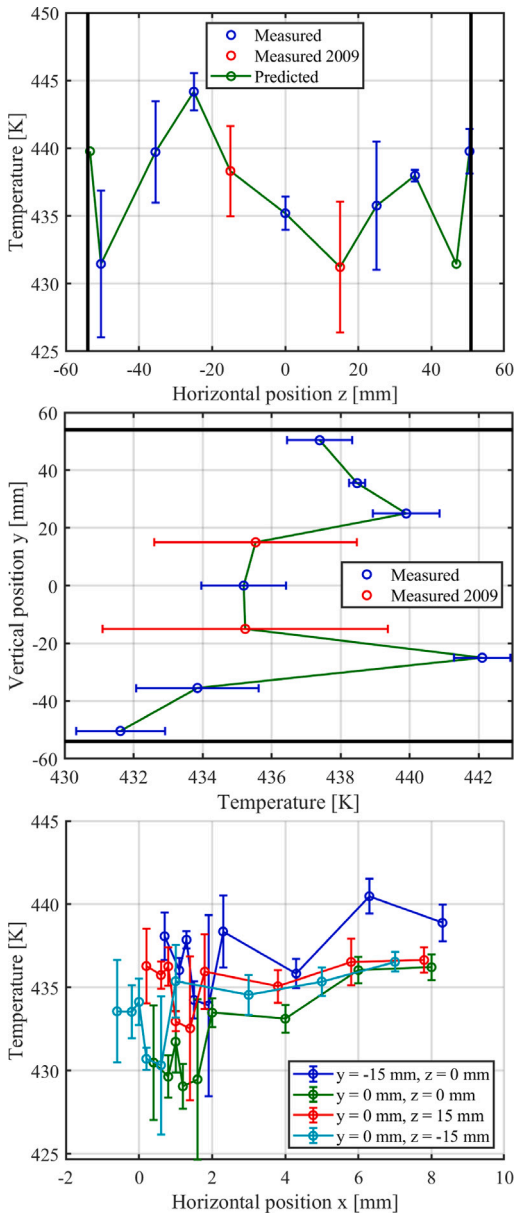

Fig. 2. Temperature distribution before the pre-burn. Error bars represent 95% confidence intervals. Top: horizontal temperature distribution at a distance of 45 mm from the injector orifice (three-thermocouple probe). Center: vertical temperature distribution at a distance of 45 mm from the injector orifice (three-thermocouple probe). Bottom: temperature distribution in the near nozzle region (five-thermocouple probe).

the most likely cause is the cooled injector tip (363 K) when compared to the heated vessel walls at 461 K. However, temperatures overall seem rather homogeneous throughout the vessel at this point. This is important, as the anticipated core density at the time of injection is based on the assumption of a uniform temperature during the filling procedure. This temperature is used in the computations to fill the vessel to a pre-selected pressure to match the core density after the pre-burn.

4.1.2. Vessel temperature evolution

The top panel of Fig. 3 shows the local temperature evolution at four different locations after the spark discharges in the top of the vessel at t = 0 s. Looking in more detail at these temperature profiles reveals several characteristic phenomena such as compression heating, flame arrival, and heat loss influences, leading to a maximum flame temperature coupled to those processes. Supplementary broadband chemiluminescence and schlieren movies of the pre-burn event are available on the ambient temperature page (for Spray A) of the ECN website [45].

The flame arrival is marked by a steep increase in temperature at the different thermocouple positions with a maximum temporal separation of approximately 200 ms in the top panel of Fig. 3. The temperature increases prior to flame arrival at the thermocouples due to compression heating when reactions are readily taking place elsewhere, and creating a pressure rise in the chamber (indicated by bulk temperature). Based on non-reacting, adiabatic compression calculations (dashed lines), slightly lower temperatures are found right before the flame arrives due to heat losses. Comparing the individual profiles shows how the temperature increase in the bottom of the vessel is reduced over the center of the vessel, presumably due to a closer proximity of the thermocouple to the vessel wall combined with the accumulation of cooler gases towards the bottom of the chamber because of buoyancy effects.

We can compare the measured temperature at these four select locations to various idealized models for the premixed combustion process. One example is an adiabatic, single-zone, constant-volume computation with all reactants at a uniform initial temperature and pressure, which predicts an equilibrium temperature of 1925 K. However, the single-zone model does not consider different compression heating and flame arrival timings for each position in the chamber. Instead, we evaluate a multi-stage model that considers a sequence of compression heating (Stage 1), constant-pressure flame (Stage 2), and then continued compression heating (Stage 3) at specific locations within the chamber. Stage 1 is compression heating prior to flame arrival (the dashed lines of Fig. 3). Stage 2 is constant-pressure, adiabatic flame computations beginning from the Stage 1 temperature. Fig. 3 shows temperature predictions ranging between 1650 K and 1800 K with dash-dotted lines for Stage 2. A constant-pressure calculation is made to consider an expected instantaneous temperature rise as the flame passes over a thermocouple with little change in overall vessel pressure.

Stage 3 is a continued temperature increase of the combustion products from Stage 2 by compression heating, once again bound by adiabatic compression. The results of this final stage are indicated by dotted lines ranging from 1830 K to 2150 K. Although it may be difficult to distinguish between the moments where the flame heats the thermocouple (Stage 2) and further heating by compression (Stage 3), the Stage 2 and Stage 3 limits provide an upper bound to idealized temperature changes from these processes. Overall, the thermocouples at the center of the vessel and at y = 26.5 mm both reach temperatures closer to those predicted by the combination of adiabatic flame computations and adiabatic compression, indicating that heat losses do not have a significant effect on the measurements in these locations. In addition, the timing of peak temperature rise at these positions corresponds to the timing of peak pressure (peak bulk temperature), suggesting that Stage 3 compression-heating dictates the maximum temperature. For the “Top” and “Bottom” thermocouple locations, the maximum temperature is reduced because of the vicinity to a cool vessel wall. Peak measured temperature in these positions also occurs prior to peak bulk temperature, indicating significant heat transfer after the initial flame arrival.

One thing that is noteworthy is the significant contrast between the single-zone, constant-volume model predictions and that of the multi-stage model discussed. The multi-stage model, which is also adiabatic, shows that mixtures that burn first and are then compressed could reach temperatures as high as 2150 K, while mixtures that burn last would reach only about 1830 K, thereby encompassing the temperature predicted for a single-zone, constant-volume calculation (1925 K). Indeed, one indication that the pre-burn should be treated within multiple, independent regions is that the measured maximum temperature for a location that was earlier to burn, but also far enough away from cold vessel boundary layers (y = 26.5 mm, z = 0) does exceed the single-zone

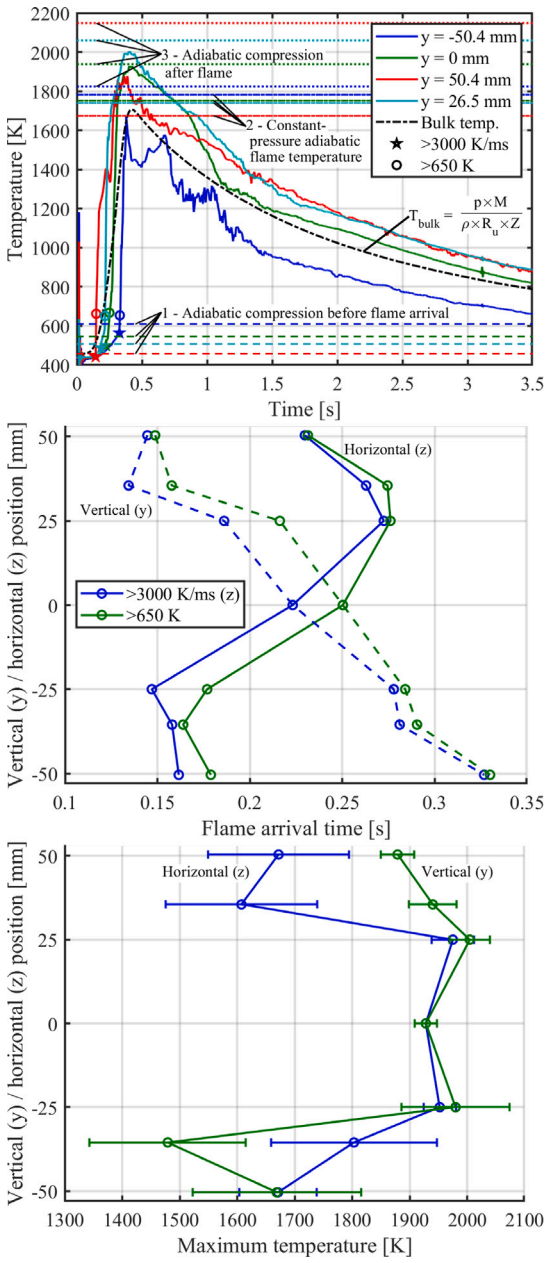

Fig. 3. Top: temperature evolution of three thermocouples at different vertical positions taken with the three-thermocouple probe. The star symbols represent the moment of flame arrival based on two different criteria. Center: flame arrival after the pre-burn at different vertical and horizontal locations in the vessel. Bottom: maximum measured temperatures with 95% confidence intervals.

temperature of 1925 K, despite non-adiabatic (heat loss) processes that tend to lower temperature. One takeaway from this discussion is that a constant-volume pre-burn vessel is not expected to produce uniform temperature combustion products shortly after flame arrival, because of the different compression histories for each location. Therefore, it is important to understand the time of flame arrival at each location, and the mixing that occurs thereafter.

The central panel of Fig. 3 shows the measured flame arrival time in the vertical (y) and horizontal (z) plane at an axial distance of 45 mm. To characterize the flame arrival, two different criteria were used: a temperature increase of 3000 K/ms, and the first time that the measured temperature exceeds 650 K. In the vertical plane (dashed line), the flame first arrives at the top-most thermocouples. The reason why the flame arrival time for y = 50.4 mm and y = 35.5 mm is so similar is the location of the spark plugs. The spark gap is located 16.5 mm below the vessel top and at a distance of 31.8 mm from the vessel centerline (i.e., at y = 37.5 mm, x = +/−31.8 mm). Therefore, the flame has to travel down (for y = 35.5 mm) or up (for y = 50.4 mm), as well as towards the centerline of the vessel (z = 0). High-speed schlieren and chemiluminescence movies in Refs. [2,45] show these early flame movements. The chemiluminescence movie (taken from below the combustion vessel) indicates that the two flames merge at the z = 0 vertical position by 0.15 s, which is in agreement with the flame arrival time measured at y = 35.5 mm. The flame continues to progress from top to bottom, reaching the bottom thermocouple location before 0.35 s, which corresponds to an overall flame speed of approximately 0.5 m/s. In the horizontal (z) plane (y = 0), the measurement points around 25 and −25 mm are the closest to the spark gaps, but the flame does not arrival at the same time on the two sides of the vessel. The difference is presumably caused by in-vessel gas motion generated by the mixing fan. The mixing fan is located in the negative z-direction side, producing higher turbulence and enhanced flame speeds on that side the chamber. Schlieren and chemiluminescence movies [2] show the flame passing the y = 0 plane by 0.15 s but also confirm that a faster flame and earlier arrival time occurs in the negative z direction. In fact, the flame arrives first at the vessel center rather than the y = 0, z = 25 mm position, despite the closer proximity to the spark plug. The growth of the flame and motion of gases inside the vessel is influenced by the fan motion, but is also most likely subject to strong buoyancy-induced flows as heat release progresses. Together, these influences combine to cause the flame to move quickly on one side of the vessel and more slowly on the other side. Note that the velocity of the gas in the chamber before ignition or at the time of injection is only on the order of 0.02 m/s [2,45], which is slow compared to the mean flame velocity (about 0.5 m/s).

The bottom panel of Fig. 3 shows the maximum temperature during the pre-burn event as a function of horizontal- and vertical position. As discussed above, the maximum temperatures in the combustion vessel are governed by the flame temperature, compression-heating effects, heat-loss effects, and gas motion. The maximum pre-burn temperature is around 2000 K, and found in the core region of the vessel in both horizontal and vertical directions. This again illustrates how the cooling effects mitigate maximum attainable temperatures towards the vessel walls. In addition, a similarity in maximum temperature for the core region suggests that mixing is active after the flame progresses. In other words, the three-stage model discussed above does not necessarily hold at all times, because of mixing between zones.

As illustrated in the top panel of Fig. 3, the different thermocouples show differences in the cool-down trend after the time of maximum temperature. Again, this is most likely governed by the internal gas flow motion caused by the pre-burn event, the mixing fan, buoyancy, and the relatively cool vessel boundaries. After 1.5 s, based on the four different thermocouple locations shown in this panel, the temperature stratification in the top of the vessel is much reduced when compared to the bottom of the vessel, which is to be expected from the counterbalancing effects of buoyancy and the cooler boundary layers. Furthermore, the ratio between the top, bottom, and core is relatively stable. This results in a reliable time period of operation between 1200 K and 700 K in which fuel can be injected with a known core-to-bulk temperature ratio [2].

4.1.3. Vessel temperature distribution after the pre-burn

Fuel is injected during the cool-down into an atmosphere with a pre-defined core temperature. As a baseline ECN condition, a core temperature of 900 K is targeted, although temperature stratification persists throughout the entire time-sequence following the pre-burn. The temperature distribution as measured by fine-wire thermocouples at a core temperature of 900 K is presented in Fig. 4, in a very similar fashion to Fig. 2.

The top panel of Fig. 4 shows the horizontal temperature stratification at an axial distance of 45 mm from the injector orifice. At a distance of 0.6 mm from the window, the temperature is heavily affected by the cooler vessel boundary layers and the mean temperature is about 150 K lower than when compared to the vessel core. The measurement point at z = −50.4 mm is located four millimeters from the vessel window, which could be somewhat influenced by the cold boundary layer. But with only a 25 K deficit compared to the core region, the protrusion into the boundary layer appears minimal.

A clear trend in the vertical temperature stratification during injection is shown in the center plot of Fig. 4. In the region that is relevant to the high-pressure fuel sprays from a single orifice injector, the effect is about 6.5 K/mm, meaning that the upper part of the lift-off length for the Spray A baseline case (see the flame structures and width of the jets, for instance, in the work by Maes et al. [46]), may be entraining gases that are 50 K hotter than those entrained in the bottom part of the spray. Especially when the flame lift-off length increases, such differences may lead to an asymmetry in the flame. This does seem to be the case, and is supported with the formaldehyde structures observed at the lowest ambient temperature in recent work [37]. The top-most measurement point in the middle panel of Fig. 4 is colder than the point immediately below it, indicating the proximity of a colder boundary layer at 4 mm from the top of the vessel. Below the center of the vessel, temperatures decrease faster until $y = -35.5$ mm, but then change little by $y = -50.4$ mm. Apparently, there is an accumulation of colder gases at the bottom of the chamber. The temperature decrease in this rather large volume at the vessel bottom (at least 15 mm) is even slightly lower than that measured in thinner boundary layers (0.6 mm from wall) at the central plane at $y = 0$ mm, z = 50.4 mm.

The bottom panel of Fig. 4 contains perhaps the most important data with respect to fuel sprays that are injected into the high-temperature core region of the vessel from the cooled vessel window that contains the fuel injector. Between two millimeters and eight millimeters, the data in the horizontal plane (y = 0 mm) is relatively constant. This behavior is consistent all the way downstream to 67 mm from the injector based on previous experiments [2]. The boundary layer when approaching the nozzle on the spray axis (green line) is visible starting at two millimeters from the orifice exit. Temperatures seem to decrease in an almost linear fashion to 830 K when approaching the closest measurement position at 0.5 mm from the injector orifice. Note that the metal tip temperature target is 363 K, but some heat-up occurs during the pre-burn, raising the inner sac temperature by 30 K (and the outer surface of the tip to an even higher temperature) [2,3]. Therefore, steep temperature gradients exist between the metal tip and the gas in this 0.5-mm gap. Interestingly, similar measurements in a rapid compression machine indicate a temperature difference of less than 50 K at a distance of approximately $x = 0.3$ mm, z = 0.3 mm (based on the axes in this work) from the injector [47]. In the cited work, experiments are even carried out during a fuel injection event. The resulting measurements show a much lower temperature (another 50 K) directly after the start of injection, indicating that boundary layer gas is indeed entrained into the jet. The authors of that study also highlight the importance of the near-nozzle boundary layer on subsequent spray behavior.

The other thermocouples on the z = +/−15 mm, $y = 0$ mm horizontal plane show a temperature decrease when approaching the injector port as well, but the decrease is less significant than at the tip. Because of the conical (18°) injector port, thermocouples at z = +/−15 mm stand away from the wall by approximately 5 mm (see Fig. 1) and are therefore farther away from the cool boundary layer than at the tip. Overall, the conical shape of the injector port is effective at minimizing the influence of the wall thermal boundary layer. For example, the region at 0.5 mm away from the injector tip is at a much higher temperature than that near (0.6 mm) the side window at an axial distance of 45 mm, despite the fact that the injector is actively cooled to 363 K while the side window is not cooled at all. Nevertheless, any temperature non-uniformity for gases that will mix with the spray may have an impact.

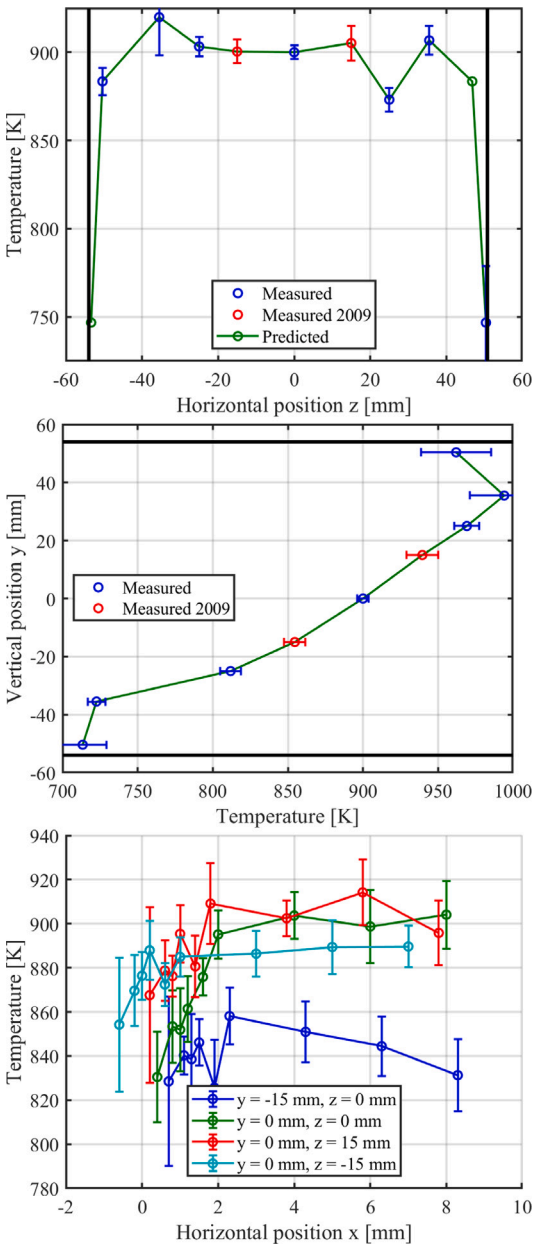

Fig. 4. Temperature distribution at the time of injection for a 900-K ambient target. Error bars represent 95% confidence intervals. Top: horizontal temperature distribution at a distance of 45 mm from the injector orifice (3-thermocouple probe). Center: vertical temperature distribution at a distance of 45 mm from the injector orifice (3-thermocouple probe). Bottom: horizontal temperature distribution in the near nozzle region (5-thermocouple probe).

Rayleigh scattering was used to provide more information on gas temperatures, particularly for gases that mix with the spray at locations where isolated thermocouple data remains sparse. A representative single-shot Rayleigh scattering image for a 900-K target ambient temperature demonstrating the technique is shown in the top panel of Fig. 5. This image is uncorrected for background flare, and regions outside of the laser light sheet are apparent, such as the spark plug ground strap at z = −32 mm, the injector port and injector tip, and inner vessel geometry (bottom left corner). In this particular example, two of the three thermocouple probes are captured in the field-of-view

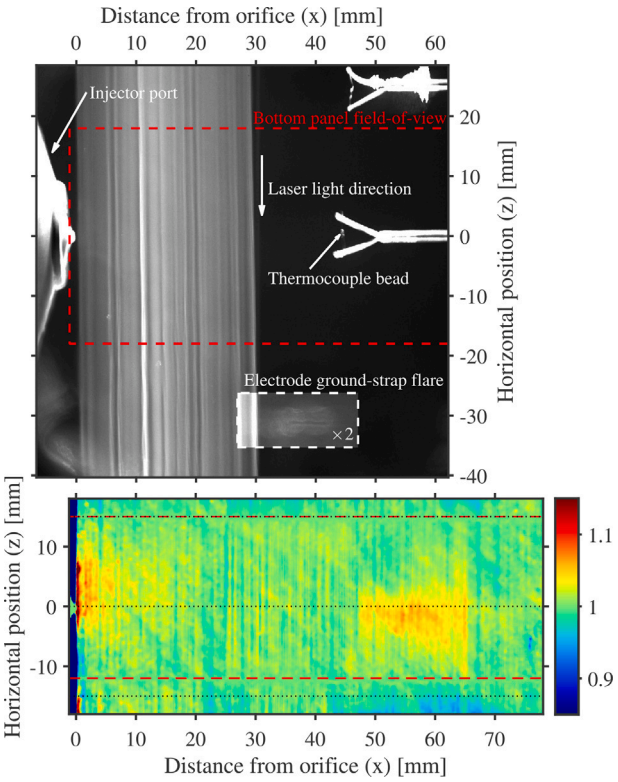

Fig. 5. Top: single raw Rayleigh scattering image showing beam-steering originating from the thermal boundary layer. The injector port with the injector tip, two thermocouple probes, the electrode ground-strap and vessel geometry in the bottom left corner are all apparent because of the laser light flare outside of the laser light sheet. Bottom: temperature distribution at the time of injection for a 900-K ambient target. The signal is inversely proportional to temperature, indicating a cool region near the injector tip at (x = 0 mm, z = 0 mm). Red dashed lines in the bottom panel indicate the reference locations where a uniform profile of 900 K was assumed, while black dotted lines correspond to the horizontal positions where thermocouple measurements were taken in the near-nozzle region.

and visualized by the laser light flare as well. The laser sheet was translated to different axial positions to provide measurements throughout entire chamber, while the thermocouples were fully retracted out of the field of view. Different background flare images were acquired and processed at each laser position as described in Section 2.3 to make the measurement quantitative.

The laser sheet propagating from top to bottom in the figure demonstrates serious non-uniformities in intensity, with growing non-uniformity in the laser sheet propagation direction. The strong striations in laser intensity in the axial direction, as well as the irregular propagation across the chamber, are created by beam steering via the thermal boundary layer at the laser-sheet entrance window. Note that these striations do not exist when the vessel is charged with gases prior to combustion, in other words, when the gases and vessel are nearly uniform in temperature and the thermal boundary layer does not exist. In addition, imaging that includes the laser-sheet entrance window at a 900-K gas temperature shows that the divergence or convergence of propagating rays originates at the window itself. These observations are consistent with the measured strong gradients in temperature at the thermal boundary layer shown by the thermocouple measurements.

The laser intensity variations obviously create a challenge for temperature quantification. However, we can use the thermocouple measurements themselves outside of the jet as calibration for temperature at those positions, and then interpolate to a 2D field. An ensemble-averaged Rayleigh scattering 2D map, which scales inversely with temperature, is shown in the bottom panel of Fig. 5. After a background correction, a reference laser sheet intensity distribution was created along the red dashed lines in the bottom panel of Fig. 5, which corresponds to the location of thermocouple measurements in this work (and those in Ref. [2]). Dividing the background-corrected signal (I) by the linearly interpolated reference laser sheet intensity (I_0) and stitching different laser sheet locations together provides the 2D distribution as shown. Note that vertical striations are indications of incompletely corrected laser intensity variations, but larger zones are regarded as significant.

As expected based on the thermocouple measurements, the Rayleigh measurements indicate a cool region ($I/I_0 > 1$) close to the injector orifice. The Rayleigh measurement results are reliable up to about 0.4 mm from the injector orifice. At this axial position, the decline in temperature is marginal at z = −15 mm and z = 15 mm according to the thermocouple measurements, but both the Rayleigh and thermocouple measurements show an approximate 10% temperature decrease immediately at the injector. Indeed, the cool region close to the injector nozzle appears to span approximately five millimeters in the negative z-direction, and ten millimeters in the positive cross-stream direction. The reason for this asymmetry could again be the bulk gas motion caused by the mixing fan.

A second cooler region seems to exist at a distance of between 48 mm and 66 mm from the injector orifice, predominantly on the mixing fan-side of the vessel. This region could be an effect of the gas being pulled towards the mixing fan in combination with buoyancy driven flows, which include the slightly lower temperature from the bottom of the vessel. As this second cooler region was not detected in the thermocouple data, it may be a remaining artifact in the Rayleigh data, such as uncorrected flare intensity. However, an alternative explanation could also be attributed to a 2-mm offset of the measurement location with the 5-thermocouple probe from the spray axis.

4.2. RANS results

RANS simulations require an initialized gas velocity, TKE, and dissipation of TKE within every cell of simulation. Gas temperature may be initialized as the mean temperature, but the RANS method includes no mechanism to initialize the temperature variance. For this reason, a method was explored to initialize gas temperature variance, as well as mean non-uniformity, within the chamber. The measured temperature distribution at the time where fuel would be injected at 900 K is used to generate the initial temperature profile imposed in the presented simulations. Fig. 6 shows the initial 3D temperature profile as well as three slices in corresponding planes. Using linear fits between the data points from Fig. 4, a 3D map containing the mean temperature and standard deviation has been generated. Then a normal distribution is used to randomly determine the temperature in each cell of the grid knowing the mean and the standard deviation. Multiple stratified initial temperature profiles can be generated using this method, by changing the seed number used to populate the normal distribution. A total of six stratified temperature profiles have been created here. In the rest of the paper, the simulations performed with a stratified initial temperature profile will be abbreviated as "non-uniform T #1 to #6 simulations", while the calculations initialized with a uniform temperature profile will be identified by the "uniform T simulation". Fig. 6 reflects the trends observed in Fig. 4 with the maximum temperature stratification in the y direction (temperature increases from the bottom to the top), and a cold zone near the injector.

4.2.1. Non-reacting simulations

The performance of the spray modeling and the impact of a non-uniform temperature profile are investigated through the study of liquid- and vapor penetrations, shown in Fig. 7. The experimental vapor penetration has been measured using schlieren imaging under inert conditions (setup details in [24]). The experimental liquid length has been measured using high-speed diffuse back-illumination imaging [48]. As recommended by the ECN [15], and applied in recent

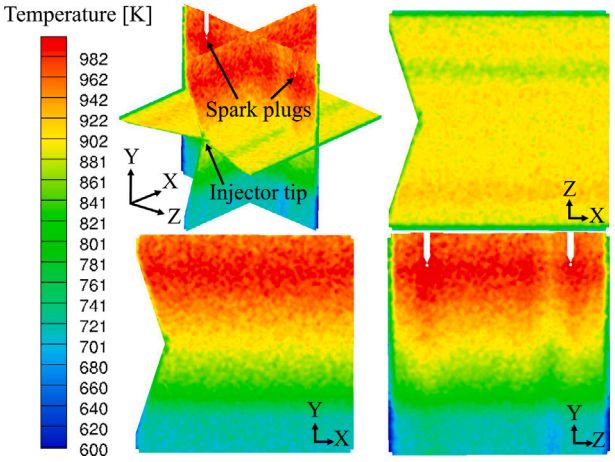

Fig. 6. Non-uniform temperature profile used to initialize the RANS simulations. The x-y and x-z planes are respectively extracted at z = 0 and $y = 0$, while the y-z plane is extracted at $x = 39.5$ mm.

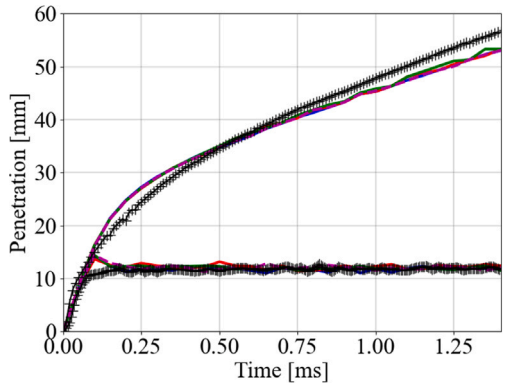

Fig. 7. Liquid length and vapor penetration comparison between RANS simulations performed with and without a uniform temperature profile and experimental values. The experimental vapor- and liquid penetration corresponds to the recent Spray A-3 injector [37].

studies (e.g., [32,38,49,50]), the liquid length in this work is defined as the furthest axial distance where the projected liquid volume (PLV) is 0.2e−3 mm^3 liquid/mm^2. The PLV is computed using the following relationship:

$$PLV = \int_{-\infty}^{\infty} LVF \cdot dz \tag{3}$$

where LVF is the liquid volume fraction defined as the percentage of liquid fuel contained within a single Eulerian cell volume. The liquid length curves in Fig. 7 show fairly good agreement between the simulations and the experiments after 0.2 ms. At 0.1 ms all simulations overestimate the experimental data. The initial temperature stratification does not influence the liquid length compared to a uniform temperature distribution in these simulations. Moreover, changing the seed number generating the stratified temperature profiles does not change the liquid penetration in any significant way either, evident from the minor differences between the non-uniform temperature curves.

The numerical vapor penetration in Fig. 7 is defined using ECN standards, which corresponds to the farthest axial distance where the mixture fraction is 0.001. The vapor penetration is close to identical for the different temperature fields. As similar penetration and mixing is expected for changes in gas temperature, provided that the ambient density is constant [24], the variances in temperature and density appear to have insignificant effects on overall mixing and penetration.

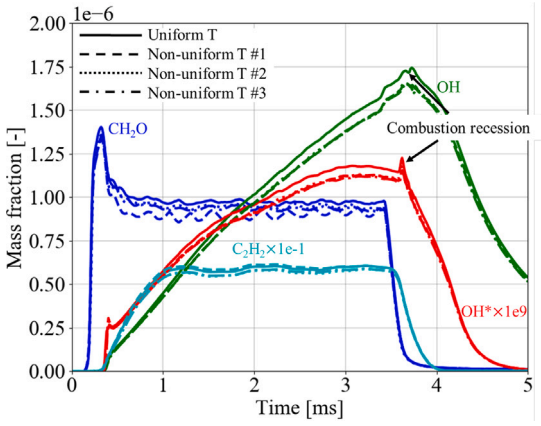

Fig. 8. Total mass fractions of four key species in the computational domain extracted from simulations performed with- and without an initial temperature profile.

The simulations vary around the experimental data, showing an over-prediction between 0.1 ms and 0.6 ms and an under-prediction after 0.6 ms. Note that the vapor penetration prediction can be improved by changing the model constants. For example, applying Pope's round jet correction has shown improvement in terms of vapor penetration in past studies [40,51]. However, it is currently beyond the scope of this paper to explore such improvements.

4.2.2. Reacting simulations

Reacting simulations, where the only change compared to the non-reacting cases is the initial oxygen concentration (15% by volume, instead of 0%) are investigated in this section.

Fig. 8 shows mass fractions for the entire domain for several important species over time for the uniform and non-uniform temperature simulations. The formaldehyde mass fraction is up to 14% lower for the non-uniform T #1 simulation compared to the uniform temperature case. The levels of OH and OH* are both 5% lower when considering an initial non-uniform temperature profile. For all simulations, the concentration of formaldehyde nearly instantaneously decreases after the end of injection, while the high-temperature combustion products (OH and OH*) keep increasing as the flame develops, peaking even after the end of injection during the combustion recession phase [52]. Finally, the C_2H_2 mass fraction trends (used as a soot precursor in many soot models [53,54]), do not show a significant dependence on the temperature stratification.

A more detailed analysis of the first- and second-stage ignition for both uniform and non-uniform temperature simulations is provided in the 2D slices of Fig. 9. The low-temperature chemistry can be observed through CH_2O species (in green), while the high-temperature flame is represented by OH species (in red). The stoichiometric mixture fraction (Z_{st} = 0.045) is represented by a white line, which has been computed using the same passive scalar definition as proposed by Tagliante et al. [38]. The low- and high-temperature evolution over time is summarized below.

At 200 μs after the start of injection (aSOI) formaldehyde appears on the fuel-rich side of the stoichiometric mixture fraction line for all the simulations. No significant difference in terms of formaldehyde mass fractions is observed between the uniform temperature case and the non-uniform temperature cases. However, the formaldehyde distribution varies between the non-uniform temperature realizations. Realization #1 contains more formaldehyde in the top branch at approximately 20 mm from the injector where temperature iso-lines of 925 K are observed. On the other hand, realization #3 shows a more homogeneous formaldehyde distribution with a corresponding more homogeneous temperature distribution at 900 K. This example

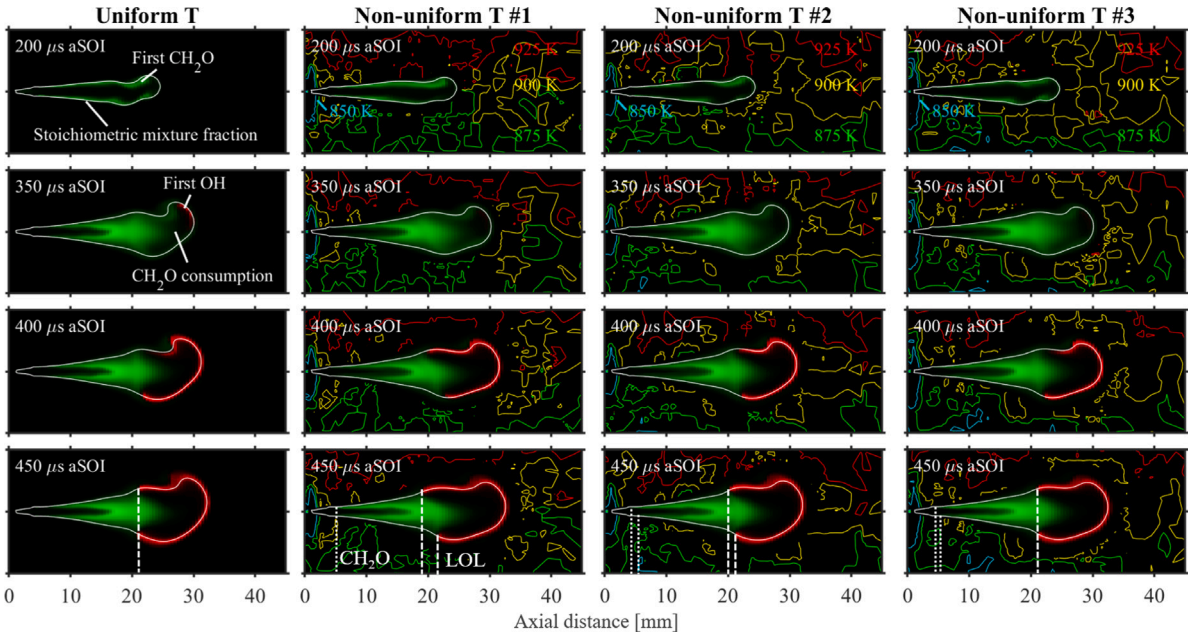

Fig. 9. Formaldehyde (green) and OH (red) mass fraction slices in the x-y plane at z = 0. The four colored lines represent different iso-temperature lines (850 K, 875 K, 900 K, and 925 K), while the white contours correspond to the stoichiometric mixture fraction.

indicates that small fluctuation in the temperature distribution can create asymmetric production of the low-temperature flame.

At 350 μs aSOI the uniform temperature case shows more pronounced formaldehyde consumption in the jet head, at the tip of which OH is present. It indicates that second stage ignition occurs earlier with a uniform temperature distribution compared to the stratified profiles.

At 400 μs aSOI, all simulations show formaldehyde in the center of the jet, while the high-temperature flame is developing on the stoichiometric line, locally consuming the low-temperature species. Interestingly, for non-uniform T #1, the upper branch of the high-temperature flame is moving closer to the injector compared to the lower branch. This behavior can be explained by the significant temperature stratification, as observed with the 925 K iso-lines near the upper branch while the lower branch propagates near a region where the temperature is 875 K. Oppositely, realizations #2 and #3 do not show such temperature stratification on both side of the spray near the high-temperature flame resulting in a more symmetric distribution of the OH mass fraction (with momentarily even an inverse trend for realization #3).

Finally, at 450 μs aSOI the low-temperature flames, and the lift-off region of the high-temperature flames, have reached a quasi-steady state. The formaldehyde cloud and the high-temperature flame base remain nearly unchanged in time. Not surprisingly, the formaldehyde cloud and the high-temperature flame base are symmetric on both sides of the spray for the uniform temperature case. It is interesting to observe that even if the mean temperature stratification is identical between the non-uniform temperature cases, varying the seed number can sometimes result in asymmetric low-temperature flame structures (#2 and #3), as illustrated with the white dashed line upstream of the formaldehyde, and sometime leads to a more symmetric formaldehyde cloud (#1). The same observation is made for the high-temperature flame, where realization #3 is much more symmetric than #1 and #2. Note that, therefore, an asymmetric low-temperature flame does not necessary result in an asymmetric high-temperature flame. Based on these results, the asymmetric behavior is mostly controlled by the local temperature stratification.

Table 2 shows a more detailed comparison of first- and second-stage ignition between the simulations and the experiments. First-stage ignition is defined following the experimental procedure proposed by Sim et al. [37], who performed high-speed formaldehyde PLIF to capture the low-temperature combustion product over time. They used the same test conditions and injector as in this study. According to their procedure, first-stage ignition is defined as the time needed for the formaldehyde signal to exceed 10% of the maximum formaldehyde PLIF intensity. For the simulations, second-stage ignition is defined as the time needed for the projected OH* mass fraction to exceed the lift-off length threshold. More details on the lift-off length threshold and the projected OH* mass fraction will be provided later in the discussion. In the non-uniform temperature cases, the first-stage ignition events is, on average, reduced by 24 μs while the second-stage ignition is delayed by 11 μs compared to the uniform temperature simulation. The delay observed for the second-stage ignition is caused by the relatively cool air entrained near the injector in the non-uniform temperature case (shown in Fig. 9 with the cyan iso-line corresponding to 850 K). Interestingly, comparing the ignition delays between the simulations and the experiments it appears that the uniform temperature simulation better predicts first-stage ignition, while second-stage ignition seems to be captured better by the non-uniform temperature cases. The lack of self-consistency with experiments suggests that improvements in combustion modeling are needed. Naturally, actions to achieve these improvements require the most accurate temperature fields as a basis.

Table 2
First and second stage ignition delay comparison between simulations performed with and without uniform temperature profile, and experiments [37].

	1st-stage ID [ms]	2nd-stage ID [ms]
Experiment	0.179	0.409
Uniform T	0.180	0.342
Non-uniform T #1	0.155	0.352
Non-uniform T #2	0.165	0.354
Non-uniform T #3	0.155	0.352
Non-uniform T #4	0.151	0.352
Non-uniform T #5	0.151	0.352
Non-uniform T #6	0.160	0.353
Non-uniform T (mean)	0.156	0.353

The asymmetric behavior of the high-temperature flame is analyzed further in Figs. 10 and 11. Fig. 10 shows spatially integrated, time-averaged (between 1 and 3 ms), projected OH* mass fraction images for

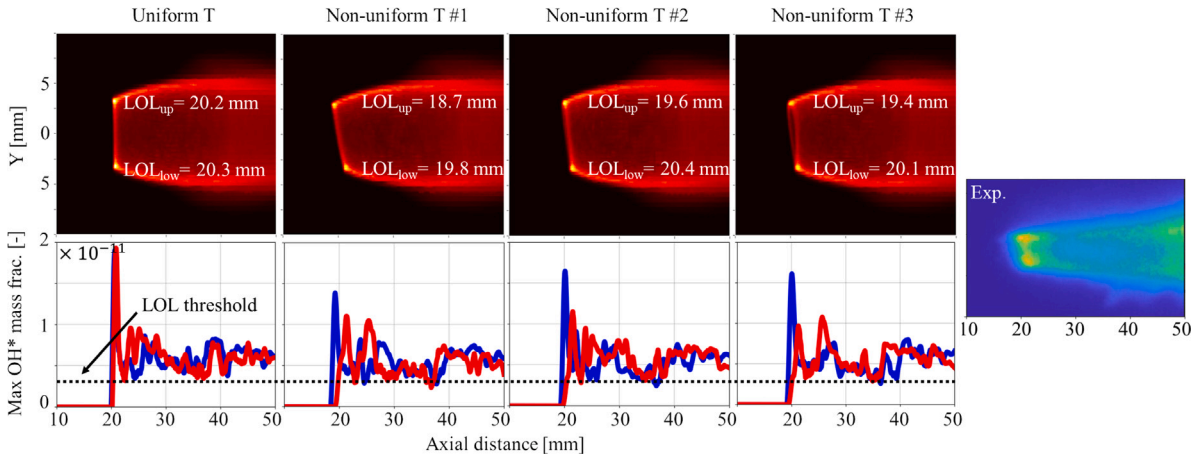

Fig. 10. Top panels: time-averaged line-of-sight projected OH* mass fraction images in the x-y plane (between 1 ms and 3 ms aSOI). Bottom: maximum line-of-sight projected OH* mass fraction in the *y* direction, along the axial distance. The blue curve covers the positive vertical location (y>0) while the red curve corresponds to the negative vertical location (y<0). The right-most panel shows an example of experimental time-averaged line-of-sight OH*.

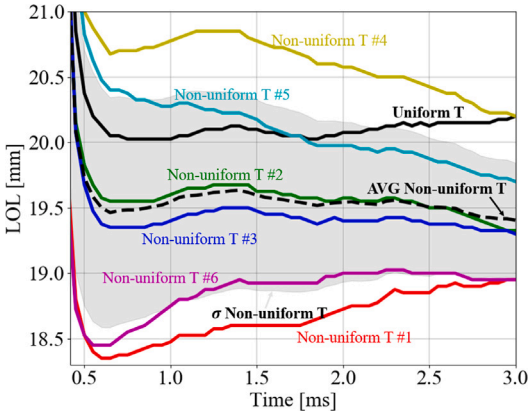

Fig. 11. Lift-off length tracking as a function of time for all the uniform and non-uniform temperature simulations.

all the simulations. The line-of-sight projected OH* is computed by integrating the OH* mass fraction in the z direction and projecting it onto the x-y plane using the same method as for the projected liquid volume, which essentially means that it is the projected OH* mass fraction per cell area. The line-of-sight projected OH* images clearly demonstrate that the lower branch for the non-uniform temperature cases is shifted downstream. Such asymmetric behavior can be explained by the vertical temperature stratification as shown with the 925-K and 875-K iso-lines in Fig. 9. If we assume that the main stabilization mechanism is auto-ignition [14,55,56], a lower temperature induces an increased ignition delay and, therefore, a flame that stabilizes farther downstream. This observation is also true if we assume flame stabilization by partially premixed flames (edge-flames) [57], since the flame speed decreases when the ambient gas temperature decreases.

Experimental measurements of the high-temperature flame, using OH* chemiluminescence, have shown asymmetric behavior between different realizations [58]. One of such examples is shown in the right-most panel of Fig. 10. The simulation panels in this figure demonstrate that the temperature fluctuations in the stratified profile on their own can cause such differences.

Quantitatively, these data can be used to compute the lift-off length (LOL) for the upper (y>0) and lower branch (y<0) independently, similar to experimental analyses. The bottom panel of Fig. 10 shows the maximum projected OH* mass fraction in the positive (blue) and negative (red) vertical direction (y) as a function of the axial direction. Following ECN procedures [15], the threshold used to detect the LOL corresponds to 50% of the leveling-off value of OH* found in the lift-off region. The upper and lower LOL are almost the same for the uniform temperature simulation, which is about 20 mm, whereas the difference between the lower and upper branches can reach up to 1.1 mm for non-uniform *T* #1. It is important to note that the presented simulations fail to correctly reproduce the exact shape of the lobes observed in experimental OH* chemiluminescence results. The lobes appear smaller and more concentrated than those found experimentally. This difference can be attributed to the RANS approach which does not capture the spatial fluctuation of the flame in time during the quasi-steady stage. Preliminary Large-Eddy Simulation results, performed under the same test conditions as this study, confirm that the projected OH* mass fraction spreads out spatially and therefore decreases in local peak concentration when the flame base fluctuates (e.g., [59]).

Using the LOL threshold found in Figs. 10, 11 shows the LOL, defined as $min(LOL_{up}, LOL_{low})$, as a function of time for all simulations. The LOL in the uniform temperature case (solid black line) stabilizes at about 70 μs, around 20 mm. For the non-uniform simulations, where LOL = LOL_{up}, most realizations show that the LOL first stabilizes around 70 μs, after which different trends are observed. In realization #3 the LOL stays fairly constant, while in realization #1 the LOL increases in time. Opposite from that, the LOL values of realizations #4 and #5 decrease over time. The ensemble-averaged LOL for the non-uniform temperature cases is shown in the dashed black line, with the shaded area representing the standard deviation. Note that the standard deviation of experimental LOL values is around 1 mm, which aligns well with the observed numerical values. The long injection duration allows for the observation that the LOL values (for all the non-uniform temperature cases) seem to converge toward a value between 19.25 mm and 19.5 mm. Indeed, if the flame first stabilizes close to the injector (realizations #1 and #6) the LOL will increase over time, whereas the opposite is observed if the flame first stabilizes far from the injector (realizations #4 and #5).

Most of the time, the injection duration is much shorter (1.54 ms for example for the standard Spray A conditions [15]). In such configuration, the high-temperature flame does not have the time to stabilize toward a value as observed in Fig. 11. At 1.5 ms, the LOL differs by approximately 2 mm between realizations #1 and #4. Pachano Prieto [60] showed a 7 mm longer LOL for the SAGE model [35] compared to the Unsteady Flamelet Progress Variable model [61,62] under uniform-temperature Spray A conditions, and while also using RANS simulations and the same chemical mechanism as in this study [36].

The combination of SAGE model and RANS CFD has typically shown LOL predictions longer than the experiment. While researchers may qualify the appropriateness of a certain combustion model based upon a match to the experiment, this study reveals that taking into account the temperature stratification can decrease the LOL by a significant amount, in a direction consistent with the experiment. Finally, it is interesting to note that despite the differences in LOL, the auto-ignition delay is very similar between the non-uniform temperature realizations, showing how these temperature stratifications to some extent decouple these combustion indicators. This is also evident from the fact that the ignition delay for the non-uniform temperature cases is longer, while the average lift-off length is shorter.

5. Summary and conclusions

The temperature distribution in a constant-volume pre-burn combustion vessel was studied experimentally using high-speed fine-wire thermocouple measurements, and single-shot Rayleigh scattering imaging. Initial vessel temperature, flame arrival, maximum flame temperature and compression heating before and after the flame arrival were identified in the time-resolved thermocouple data. Temperature data in different boundary layers is collected at the time of injection using the thermocouple point measurements. A full 2D temperature distribution in the horizontal plane of the fuel injector, until 0.4 mm from the injector orifice is obtained through the use of Rayleigh scattering. To identify the impact of the characterized temperature distribution, representative RANS simulations were carried out using the CONVERGE CFD code, version 3.0. The simulations consisted of a uniform temperature reference case, and six different stratified temperature realizations. In these six cases, the mean temperature stratification determined in the experiments was randomly superimposed by the variance found in those experiments. Based on the experimental and numerical results presented in this study, the following conclusions were drawn:

- The vessel temperature after the filling procedure and preceding the spark is relatively homogeneous within a range of about ten degrees. Therefore, density assumptions based on a target fill-pressure are valid, granted that the core-to-bulk ratio at the moment of fuel injection is respected.
- The temperature history during the pre-burn event depends on compression heating, flame temperature, buoyancy, heat losses to the wall, and mixing fan-induced gas motion. Measured temperatures close to the center of the vessel are close to what is expected from adiabatic compression before and after an adiabatic flame computation, while significant heat losses are noticed closer to the vessel walls.
- With the time it takes for the turbulent flame to consume all the fresh charge gases, a large-scale gas motion accompanied by significant temperature fluctuations is created. After about 1.5 s, the gases stabilize resulting in a stable and repeatable window of operation from 1200 K down to 700 K for studying (reacting) fuel jets.
- At the ECN baseline ambient temperature target condition of 900 K for n-dodecane fuel sprays, and with a fuel injector mounted to protrude into the chamber and away from the wall, a relatively homogeneous distribution is found in the horizontal plane, starting from about 2 mm from the injector orifice. Close to the injector orifice, local temperatures decrease by values close to 100 K in a relatively linear trend when approaching the injector. In the vertical plane, temperatures decrease by about 6.5 K/mm in the center of the vessel.
- Using a small sub-set of chemical reactions, OH^* species were added to the Yao mechanism. With this addition, bright OH^* lobes were observed, similar to experimental observations. Therefore, these results were deemed more suitable for a direct comparison.
- The influence of the non-uniform temperature field showed no significant influence on the liquid- and vapor penetration. Low- and high-temperature ignition delay, however, were advanced by 24 μs and delayed by 11 μs, respectively, due to the thermal stratification and cold boundary layer near the injector tip. Because of this vertical temperature stratification, a lift-off length difference of up to 1.1 mm was detected between the bottom and the top of the flame in one of the realizations. Similarly, an asymmetry of the formaldehyde structure was observed in most cases.
- The lift-off length of different cases with a non-uniform temperature simulations was tracked over time. The average trend is that these cases have a shorter lift-off length, despite a slightly increased ignition delay, compared to the uniform temperature case. For individual events, those with a LOL that was longer than the mean decreased over time, while the short-LOL cases showed the opposite. Therefore, all cases seemed to converge towards an ultimate LOL value given sufficient time.

CRediT authorship contribution statement

Noud Maes: Conceptualization, Methodology, Software, Validation, Formal analysis, Data curation, Writing – original draft, Visualization. **Fabien Tagliante:** Conceptualization, Methodology, Software, Validation, Formal analysis, Investigation, Data curation, Writing – original draft, Visualization. **Hyung Sub Sim:** Validation, Investigation, Formal analysis, Writing – review & editing. **Maarten Meijer:** Validation, Investigation, Formal analysis, Data curation. **Julien Manin:** Validation, Investigation, Formal analysis, Data curation, Writing – review & editing. **Lyle M. Pickett:** Conceptualization, Methodology, Software, Validation, Resources, Writing – review & editing, Supervision, Project administration, Funding acquisition.

Declaration of competing interest

The authors declare that they have no known competing financial interests or personal relationships that could have appeared to influence the work reported in this paper.

Data availability

Temperature distribution files, as well as experimental and numerical data can be accessed via the ECN website links provided in the references. Further data can be made available on request.

Acknowledgments

The experiments were conducted at the Combustion Research Facility, Sandia National Laboratories, Livermore, CA. This Article has been authored by National Technology and Engineering Solutions of Sandia, LLC. under contract No. DE-NA0003525 with the U.S. Department of Energy/National Nuclear Security Administration. The United States Government retains and Elsevier, by accepting the article for publication, acknowledges that the United States Government retains a non-exclusive, paid-up, irrevocable, world-wide license to publish or reproduce the published form of this manuscript, or allow others to do so, for United States Government purposes. Chris Carlen, Keith Penney, and Dave Cicone are gratefully acknowledged for technical assistance at Sandia. Nick Killingsworth and William J. Pitz at Lawrence Livermore National Laboratory are gratefully acknowledged for their help with the chemical mechanism. The authors also wish to thank Gurpreet Singh and Michael Weismiller, program managers at U.S. DOE, for their support.

Table A.3
Elementary reactions to model OH^* formation and quenching.

Reaction	A	n	E_a
$CH+O_2 \leftrightarrow OH^*+CO$	4.80E+16	−1.0	5100.0
$H+O+M \leftrightarrow OH^*+M$	3.80E+14	0.0	10000.0
$H+2OH \leftrightarrow OH^*+H_2O$	1.45E+15	0.0	0.0
$OH^*+Ar \leftrightarrow OH+Ar$	2.170E+10	0.5	2057.0
$OH^*+H_2O \leftrightarrow OH+H_2O$	5.920E+12	0.5	−861.0
$OH^*+CO_2 \leftrightarrow OH+CO_2$	2.750E+12	0.5	−968.0
$OH^*+CO \leftrightarrow OH+CO$	3.230E+12	0.5	−787.0
$OH^*+H \leftrightarrow OH+H$	1.500E+12	0.5	0.0
$OH^*+H_2 \leftrightarrow OH+H_2$	2.950E+12	0.5	−444.0
$OH^*+O_2 \leftrightarrow OH+O_2$	2.100E+12	0.5	−482.0
$OH^*+O \leftrightarrow OH+O$	1.500E+12	0.5	0.0
$OH^*+OH \leftrightarrow 2OH$	1.500E+12	0.5	0.0
$OH^*+CH_4 \leftrightarrow OH+CH_4$	3.360E+12	0.5	−635.0
$OH^* \leftrightarrow OH+h\nu$	1.400E+06	0.0	0.0
$OH^*+N_2 \leftrightarrow OH+N_2$	1.080E+11	0.5	−1238.0

Appendix A

The OH^* reactions available in the Aramco 2.0 mechanism [63] have been added to the Yao mechanism [36] in this work. Table A.3 shows the elementary reactions used to model OH^* with their corresponding rate coefficients, which are expressed as:

$$k = AT^n e^{-E_a/RT}, \tag{A.1}$$

where the units of the A, E_a, R, and T are $cm^6mol^{-2}s^{-1}K^{-1}$, $mol^{-1}cal$, $mol^{-1}K^{-1}cal$, and K, respectively.

Appendix B. Supplementary data

Supplementary material related to this article can be found online at https://doi.org/10.1016/j.expthermflusci.2023.110866.

References

[1] R.S.G. Baert, P.J.M. Frijters, L.M.T. Somers, C.C.M. Luijten, et al., Design and Operation of a High Pressure, High Temperature Cell for HD Diesel Spray Diagnostics: Guidelines and Results, SAE Technical Paper 2009-01-0649, 2009.

[2] L.M. Pickett, C.L. Genzale, G. Bruneaux, L. Malbec, et al., Comparison of Diesel Spray Combustion in Different High-Temperature, High-Pressure Facilities, SAE Technical Paper 2010-01-2106, 2010.

[3] M. Meijer, L.M.T. Somers, J. Johnson, J. Naber, et al., Engine Combustion Network (ECN): Characterization and Comparison of Boundary Conditions for Different Combustion Vessels, Atom. Spray 22 (9) (2012) 777–806.

[4] M. Bardi, R. Payri, L.M. Malbec, G. Bruneaux, et al., Engine Combustion Network (ECN): Comparison of Spray Development, Vaporization, and Combustion in Different Combustion Vessels, Atom. Spray 22 (10) (2012) 807–842.

[5] D. Siebers, Ignition delay characteristics of alternative diesel fuels: Implications on cetane number, SAE Trans. 94 (7) (1985) 673–686.

[6] J. Naber, D. Siebers, Effects of Gas Density and Vaporization on Penetration and Dispersion of Diesel Sprays, SAE Technical Paper 960034, 1996.

[7] D. Verhoeven, J. Vanhemelryck, T. Baritaud, Macroscopic and Ignition Characteristics of High-Pressure Sprays of Single-Component Fuels, SAE Technical Paper 981069, 1998.

[8] S. Som, P.K. Senecal, E. Pomraning, Comparison of RANS and LES turbulence models against constant volume diesel experiments, in: ILASS-Americas 24rd Annual Conference, 2012.

[9] S. Bhattacharjee, D.C. Haworth, Simulations of transient n-heptane and n-dodecane spray flames under engine-relevant conditions using a transported PDF method, Combust. Flame 160 (2013) 2083–2102.

[10] U. Egüz, S. Ayyapureddi, C. Bekdemir, B. Somers, et al., Manifold resolution study of the FGM method for an igniting diesel spray, Fuel 113 (2013) 228–238.

[11] J.M. Desantes, J.M. García-Oliver, J.M. Pastor, A. Pandal, et al., Coupled/decoupled spray simulation comparison of the ECN spray a condition with the Σ-Y Eulerian atomization model, Int. J. Multiphase Flow 80 (2016) 89–99.

[12] R.N. Dahmsand G.A. Paczko, S.A. Skeen, L.M. Pickett, Understanding the ignition mechanism of high-pressure spray flames, Proc. Combust. Inst. 36 (2017) 2615–2623.

[13] H. Kahila, A. Wehfrfritz, O. Kaario, M.G. Masouleh, et al., Large-eddy simulation on the influence of injection pressure in reacting Spray A, Combust. Flame 191 (2018) 142–159.

[14] L.M. Pickett, S. Kook, T.C. Williams, Visualization of Diesel Spray Penetration, Cool-Flame, Ignition, High-Temperature Combustion, and Soot Formation Using High-Speed Imaging, SAE Int. J. Engines 2 (2009) 439–459.

[15] L.M. Pickett, 2022. Available at https://www.ecn.sandia.gov.

[16] J.E. Dec, Advanced compression-ignition engines–understanding the in-cylinder processes, Proc. Combust. Inst. 32 (2009) 2727–2742.

[17] L. Malbec, G. Bruneaux, Study of Air Entrainment of Multi-hole Diesel Injection by Particle Image Velocimetry - Effect of Neighboring Jets Interaction and Transient Behavior After End of Injection, SAE Int. J. Engines 3 (2010) 107–123.

[18] W.E. Eagle, M.P.B. Musculus, L.M.C. Malbec, G. Bruneaux, An Improved Entrainment Rate Measurement Method for Transient Jets from 10 kHz Particle Image Velocimetry, Atom. Sprays 27 (2017) 531–557.

[19] P. Sphicas, L.M. Pickett, S.A. Skeen, J. Frank, Engine combustion network sandia combustion vessel velocity stratification webpage, 2022, https://Ecn.Sandia.Gov/Velocity-Distribution/.

[20] L. Malbec, G. Bruneaux, B. Somers, C. Rouselle, et al., Identifying the Driving Processes of Diesel Spray Injection through Mixture Fraction and Velocity Field Measurements at ECN Spray A, SAE Technical Paper 2020-01-0831, 2020.

[21] P.R.N. Childs, J.R. Greenwood, C.A. Long, Review of temperature measurement, Rev. Sci. Instr. 71 (2000).

[22] C. Espey, J.E. Dec, T.A. Litzinger, D.A. Santavicca, Planar Laser Rayleigh Scattering for Quantitative Vapor-Fuel Imaging in a Diesel Jet, Combust. Flame 109 (1997) 65–86.

[23] C.A. Idicheria, L.M. Pickett, Quantitative Mixing Measurements in a Vaporizing Diesel Spray by Rayleigh Imaging, SAE Technical Paper 2007-01-0647, 2007.

[24] L.M. Pickett, J. Manin, C.L. Genzale, D.L. Siebers, et al., Relationship between diesel fuel spray vapor penetration/dispersion and local fuel mixture fraction, SAE Int. J. Engines 2 (2011) 764–799.

[25] L.M. Pickett, Engine Combustion Network Sandia Combustion Vessel Geometry, 2022, https://Ecn.Sandia.Gov/Diesel-Spray-Combustion/Sandia-Cv/Combustion-Vessel-Geometry/2009-To-Present/.

[26] D. Siebers, Liquid-Phase Fuel Penetration in Diesel Sprays, SAE Technical Paper 980809, 1998.

[27] D. Siebers, B. Higgins, Flame Lift-Off on Direct-Injection Diesel Sprays Under Quiescent Conditions, SAE Technical Paper 2001-01-0530, 2001.

[28] J.C. Beale, R.D. Reitz, Modeling Spray Atomization with the Kelvin-Helmholtz/Rayleigh-Taylor Hybrid Model, Atom. Sprays 9 (1999) 623–650.

[29] P. Senecal, K. Richards, E. Pomraning, T. Yang, et al., A New Parallel Cut-Cell Cartesian CFD Code for Rapid Grid Generation Applied to In-Cylinder Diesel Engine Simulations, SAE Technical Paper 2007-01-0159, 2007.

[30] A. Amsden, T. Butler, P. O'Rourke, The KIVA-II Computer Program for Transient Multidimensional Chemically Reactive Flows with Sprays, SAE Technical Paper 872072, 1987.

[31] N. Frössling, Über die Verdunstung fallender Tropfen, Gerlands Beiträge Geophys. 52 (1938) 170–216.

[32] T.M. Nguyen, R.N. Dahms, L.M. Pickett, F. Tagliante, The Corrected Distortion model for Lagrangian spray simulation of transcritical fuel injection, Int. J. Multiphase Flow 148 (2022) 103927.

[33] D.P. Schmidt, C.J. Rutland, A New Droplet Collision Algorithm, J. Comp. Phys. 164 (2000) 62–80.

[34] A. Liu, D. Mather, R. Reitz, Modeling the Effects of Drop Drag and Breakup on Fuel Sprays, SAE Technical Paper 930072, 1993.

[35] P. Senecal, E. Pomraning, K. Richardsas, T. Briggs, et al., Multi-Dimensional Modeling of Direct-Injection Diesel Spray Liquid Length and Flame Lift-off Length using CFD and Parallel Detailed Chemistry, SAE Technical Paper 2003-01-1043, 2003.

[36] T. Yao, Y. Pei, B. Zhong, S. Som, et al., A compact skeletal mechanism for n-dodecane with optimized semi-global low-temperature chemistry for diesel engine simulations, Fuel 191 (2017) 339–349.

[37] H.S. Sim, N. Maes, L. Weiss, L.M. Pickett, et al., Detailed Measurements of Transient Two-Stage Ignition and Combustion Processes in High-Pressure Spray Flames using Simultaneous High-Speed Formaldehyde PLIF and Schlieren Imaging, Proc. Combust. Inst. 38 (2021) 5713–5721.

[38] F. Tagliante, H. Sim, L. Pickett, T. Nguyen, et al., Combined Experimental/Numerical Study of the Soot Formation Process in a Gasoline Direct-Injection Spray in the Presence of Laser-Induced Plasma Ignition, SAE Technical Paper 2020-01-0291, 2020.

[39] E. Pomraning, K. Richards, P. Senecal, Modeling Turbulent Combustion Using a RANS Model, Detailed Chemistry, and Adaptive Mesh Refinement, SAE Technical Paper 2014-01-1116, 2014.

[40] J.M. Desantes, J.M. García-Oliver, R. Novella, E.J. Pérez-Sánchez, Application of an unsteady flamelet model in a RANS framework for spray A simulation, App. Therm. Eng. 117 (2017) 50–64.

[41] Y. Pei, S. Som, E. Pomraning, P.K. Senecal, et al., Large eddy simulation of a reacting spray flame with multiple realizations under compression ignition engine conditions, Combust. Flame 162 (2015) 4442–4455.

[42] Y. Li, C. Zhou, K.P. Somers, K. Zhang, et al., The oxidation of 2-butene: A high pressure ignition delay, kinetic modeling study and reactivity comparison with isobutene and 1-butene, Proc. Combust. Inst. 36 (2017) 403–411.

[43] A. Varna, A. Wehrfritz, E.R. Hawkes, M.J. Cleary, et al., Application of a multiple mapping conditioning mixing model to ECN Spray A, Proc. Combust. Inst. 37 (2019) 3263–3270.
[44] L.M. Pickett, Engine Combustion Network Sandia Combustion Vessel Ambient Composition Webpage, 2022, https://Ecn.Sandia.Gov/Diesel-Spray-Combustion/Sandia-Cv/Ambient-Conditions/.
[45] L.M. Pickett, Engine Combustion Network Sandia Combustion Vessel Thermal Distribution Movies, 2022, https://Ecn.Sandia.Gov/Diesel-Spray-Combustion/Sandia-Cv/Thermal-Distribution/Thermal-Distribution-for-Spray-A/.
[46] N. Maes, M. Meijer, N. Dam, B. Somers, et al., Characterization of Spray A flame structure for parametric variations in ECN constant-volume vessels using chemiluminescence and laser-induced fluorescence, Combust. Flame 174 (2016) 138–151.
[47] M. Ben Houidi, C. Hespel, M. Bardi, O. Nilaphai, et al., Characterization of the ECN spray A in different facilities. Part 1: boundary conditions characterization, Rev. IFP Energies Nouvelles 75 (2020).
[48] F.R. Westlye, K. Penney, A. Ivarsson, L.M. Pickett, et al., Diffuse back-illumination setup for high temporally resolved extinction imaging, Appl. Opt. 56 (17) (2017) 5028–5038.
[49] J. Hwang, K. Yasutomi, M. Arienti, L. Pickett, Numerical Investigation of Near Nozzle Flash-Boiling Spray in an Axial-Hole Transparent Nozzle, SAE Technical Paper 2020-01-0828, 2020.
[50] N. Maes, S.A. Skeen, M. Bardi, R.P. Fitzgerald, et al., Spray Penetration, Combustion, and Soot Formation Characteristics of the ECN Spray C and Spray D Injectors in Multiple Combustion Facilities, Appl. Therm. Eng. 172 (2020) 1–14.
[51] S.B. Pope, An explanation of the turbulent round-jet/plane-jet anomaly, A.I.A.A. J. 16 (1978) 279–281.
[52] B. Knox, C. Genzale, L. Pickett, J. Garcia-Oliver, et al., Combustion Recession after End of Injection in Diesel Sprays, SAE Technical Paper 2015-01-0797, 2015.
[53] H. Hiroyasu, T. Kadota, Models for Combustion and Formation of Nitric Oxide and Soot in Direct Injection Diesel Engines, SAE Technical Paper 760129, 1976.
[54] K.M. Leung, R.P. Lindstedt, A simplified reaction mechanism for soot formation in nonpremixed flames, Combust. Flame 87 (1991) 289–305.
[55] C. Pauls, G. Grünefeld, S. Volgel, N. Peters, Combined Simulations and OH-Chemiluminescence Measurements of the Combustion Process using Different Fuels under Diesel-Engine like Conditions, SAE Technical Paper 2007-01-0020, 2007.
[56] F. Tagliante, T. Poinsot, L.M. Pickett, P. Pepiot, et al., A conceptual model of the flame stabilization mechanisms for a lifted Diesel-type flame based on direct numerical simulation and experiments, Combust. Flame 201 (2019) 65–77.
[57] D.K. Dalakoti, B. Savard, E.R. Hawkes, A. Wehrfritz, et al., Direct numerical simulation of a spatially developing n-dodecane jet flame under Spray A thermochemical conditions: Flame structure and stabilisation mechanism, Combust. Flame 217 (2020) 57–76.
[58] F. Tagliante, T.M. Nguyen, M.P. Dhanji, H.S. Sim, et al., The role of cool-flame fluctuations in high-pressure spray flames, studied using high-speed optical diagnostics and Large-Eddy Simulations, Proc. Combust. Inst. (2022) in press.
[59] E. Hawkes, ECN2 Presentation on Lift-Off Length, 2022, https://Ecn.Sandia.Gov/Ecn-Workshop/Ecn2-Proceedings/.
[60] L.M. Pachano Prieto, CFD modeling of combustion and soot production in Diesel sprays (Ph.D. thesis), Universitat Politècnica de València, 2020.
[61] J.F. Winklinger, Implementation of a Combustion Model Based on the Flamelet Concept and Its Application to Turbulent Reactive Sprays (Ph.D. thesis), Universitat Politècnica de València, 2014.
[62] E.J. Perez Sanchez, Application of a Flamelet-Based Combustion Model to Diesel-like Reacting Sprays (Ph.D. thesis), Universitat Politècnica de València, 2018.
[63] X. Li, Z. Xu, C. Guan, Z. Huang, Impact of exhaust gas recirculation (EGR) on soot reactivity from a diesel engine operating at high load, App. Therm. Eng. 68 (2014) 100–106.